J Mater Sci: Mater Electron **(2024) 35:469**

Novel PANI:Borophene/Si Schottky device for the sensitive detection of illumination and NaCl salt solutions

D. E. Yıldız[1,*], S. Karadeniz[2], M. Yıldırım[3], N. Tasaltın[4,5,6,7], A. Gulsaran[8,9], B. Bastug Azer[8,9], and M. Yavuz[8,9]

[1] *Department of Physics, Faculty of Arts and Sciences, Hitit University, 19030 Çorum, Turkey*
[2] *Department of Energy Systems Engineering, Faculty of Engineering, Giresun University, 28000 Giresun, Turkey*
[3] *Department of Biotechnology, Faculty of Science, Selcuk University, 42130 Konya, Turkey*
[4] *Environment and Energy Technologies Research Center, Maltepe University, Istanbul, Turkey*
[5] *Department of Basic Sciences, Maltepe University, Istanbul, Turkey*
[6] *Department of Renewable Energy Technologies and Management, Maltepe University, Istanbul, Turkey*
[7] *CONSENS Inc., Maltepe University Research Center, Technopark Istanbul, Istanbul, Turkey*
[8] *Waterloo Institute for Nanotechnology (WIN), University of Waterloo, Waterloo, ON, Canada*
[9] *Mechanical and Mechatronic Engineering Department, University of Waterloo, Waterloo, ON, Canada*

Received: 3 December 2023
Accepted: 20 February 2024
Published online: 29 February 2024

© The Author(s), 2024

ABSTRACT

Metal/semiconductor structures, particularly Schottky diodes, play a crucial role in semiconductor identification and the production of electronic devices, like solar cells, photodetectors, photodiodes, and field-effect transistors (FETs). These structures are of great interest due to their ability to modify electrical and optical properties, responding to external factors such as illumination and temperature. However, despite extensive research in this field, there has been limited exploration of silicon-based metal/semiconductor structures incorporating PANI:Borophene interfacial materials. In this study, we prepared PANI:Borophene/p-Si and PANI:Borophene/n-Si structures and examined their photodiode properties using various measurements. The unoccupied trap levels (m) obtained 0.44 and 0.33 for Al/PANI:Borophene/p-Si and Au/PANI:Borophene/n-Si device, respectively. Our investigation revealed that both structures exhibited rectification behavior, with linear characteristics in the forward bias region, and deviations attributed to series resistance effects at higher voltages. Moreover, the presence of borophene in the interfacial layer led to improvements in the devices' electrical properties. Finally, the PANI:Borophene/Si Schottky diodes was tested for salt detection and the Al/PANI:Borophene/p-Si diode has the characteristics of salt (NaCl) concentration

Our findings suggest the potential for PANI:Borophene-based photodiodes with enhanced photoresponse properties. The experimental results showed that the produced devices exhibited photovoltaic attitude and hence can be candidates for opto-electronic applications.

Address correspondence to E-mail: desrayildiz@hitit.edu.tr

https://doi.org/10.1007/s10854-024-12243-x

detection sensor and it successfully detected salt concentration changes with respect to current flow.

1 Introduction

Metal/semiconductor structures (Schottky diode) have become an important tool in the identification of semiconductors. Schottky diodes and similar metal/semiconductor structures are widely used in various experiments to assess the properties of semiconductor materials. These structures provide information about the electrical properties, carrier lifetimes, surface conditions, and other characteristics of semiconductor materials. In particular, Schottky diodes are utilized to examine the electrical properties of semiconductor surfaces. The current–voltage (*I–V*) characteristics of Schottky diodes can be correlated with factors, such as the surface condition, surface area, and surface cleanliness of the semiconductor. Therefore, Schottky diodes are commonly employed as a tool to comprehend the structural and electrical properties of semiconductor materials, because these structures play a critical role in the production of important electronic devices, such as solar cells, photodetectors, photodiodes and field-effect transistors (FET) [1].

Schottky diodes have rectifying properties like p-n junctions and consist of a metal and semiconductor with a region where active charges occur [2–4]. "p"- or "n"-type semiconductor materials can be used in the production of Schottky diodes.

In Schottky junctions, the interface layer between the semiconductor and metal is an effective layer that influences the diode's performance, stability, and dependability. Interface states are induced by the location of the electrical charges present in the interface as well as its composition, quality, and non-stoichiometric structure. The image force lowering effect is the main parameter influenced by Schottky barrier inhomogeneities. The metal–semiconductor barrier is lowered as a result of image force interaction with the field at their interface, a phenomenon known as image force lowering [3]. In addition to these junctions, many researchers are also interested in organic or inorganic interfaces that can change the electrical and optical properties of these devices. Performance parameters of metal/semiconductor contacts can be varied as a function of various external factors, such as illumination and temperature. For this reason, studies in this field have always been attractive.

It is very important to detect light with a device and use it in industrial applications. On the other hand, with the increasing energy need, studies continue to convert light into electrical energy in a low-cost and efficient way [5–9]. These devices are called photodiodes, and can convert light into current or electrical signals or detect it. On the other hand, metal/semiconductor structures with interface layers are very important in creating photodiodes due to their material diversity and applicability. In this field, devices consisting of p-type and n-type silicon ground conductors and thin-film connections are mostly used [10]. Although both silicon and germanium are generally used in semiconductor devices, the current trend is to use silicon. At room temperature, a silicon crystal has fewer free electrons than a germanium crystal. This means that silicon will have much smaller collector cut-off current than germanium. Silicone has a higher operating temperature. Therefore, silicone devices are not easily damaged by excessive heat. Peak reverse voltage values of silicon diodes are larger than germanium diodes. For this reason, Si is the most preferable semiconducting material in that field.

The interfacial layers are important factors that determine the usage areas of metal/semiconductor devices. Therefore, different inorganic and organic interface layers are used for material diversity and applicability. Some researchers have conducted research on visible and ultraviolet photodiodes with interfacial layers. Gozeh et al. have reported the Zn-doped CdO interlayers in Al/Zn–CdO/p-Si/Al photodiodes, with their electrical and optical attributes [11]. Çetinkaya et al. have reported Photovoltaic characteristics of Au/PVA (Bi-doped)/n-Si Schottky photodiodes [12]. In addition, metal oxides such as TiO_2, Ga_2O_3, and WO_3 have a wide band gap and are generally used to detect ultraviolet light [13–15]. Zinc oxide (ZnO), an inorganic compound with a wide and direct band gap, is also promising material for opto-electronic applications [16–18].

Polyaniline (PANI), which has many advantages, is the material that attracts the most attention among various conductive polymers. Because it is cheap, simple to prepare, resistant to oxidation and has controllable properties. Electrical properties can also be changed by doping [19–21]. In recent years, two-dimensional

materials such as grapheme [22], silicene [23–25], germanene [26], phosphorene [27], arsenene [28], and antimonene [29] have received increasing attention from researchers. Many two-dimensional materials have been synthesized by researchers or their theoretical predictions have been made [30]. In addition to their unique physical and chemical properties, two-dimensional materials have linear band structures close to the Fermi level and high electrical and thermal conductivity. Therefore, they have a wide potential for use in electronic devices and energy storage [30]. Borophene is an atomic monolayer of boron crystal and has a two-dimensional allotrope. Many experiments and theoretical studies have been reported on many properties of borophene, such as its electronic structure, superconductivity and mechanical features, optical properties, thermal conductivity of lattice, atomic adsorption, and reactivity of surface [31–38]. Borophene has shown wide application potential as an anode material in metal ion batteries, thanks to its high capacity and excellent electronic and ionic conductivity properties, as well as some unique physical and chemical properties [30].

As it is known, oceans are the largest water resource in the world and are extremely important for human life. Today, determining the salinity of oceans, which have rich minerals and nutrients necessary for human life, is used to monitor the ocean environment and climate [39]. Because of changing in seawater salinity cause the formation of water masses and stratification in the ocean and the formation of internal ocean waves [40–42]. For this reason, studies on measuring seawater salinity have gained momentum in recent years [43–47], and the salinity of seawater is measured according to electrical conductivity, which is based on the relationship between ion content and conductivity [48].

Many studies on metal/semiconductor photodiodes created using different interface layers have been presented in the literature [49–52]. To our knowledge, no study has yet been reported on the a silicon-based metal/semiconductor structure consisting of PANI:Borophene interfacial material. In this context, PANI:Borophene/p-Si and PANI:Borophene/n-Si structures have been prepared and their photodiode properties have been examined using various measurements. Also, the PANI:Borophene/Si Schottky diodes have tested for salt detection. We believe that the results obtained in this novel study will potentially benefit further research.

2 Experimental details

2.1 Synthesis of PANI:Borophene and structural properties

The preparation stages of the exfoliated borophene was previously reported in literature [53–56] and this process can be seen in Fig. 1.

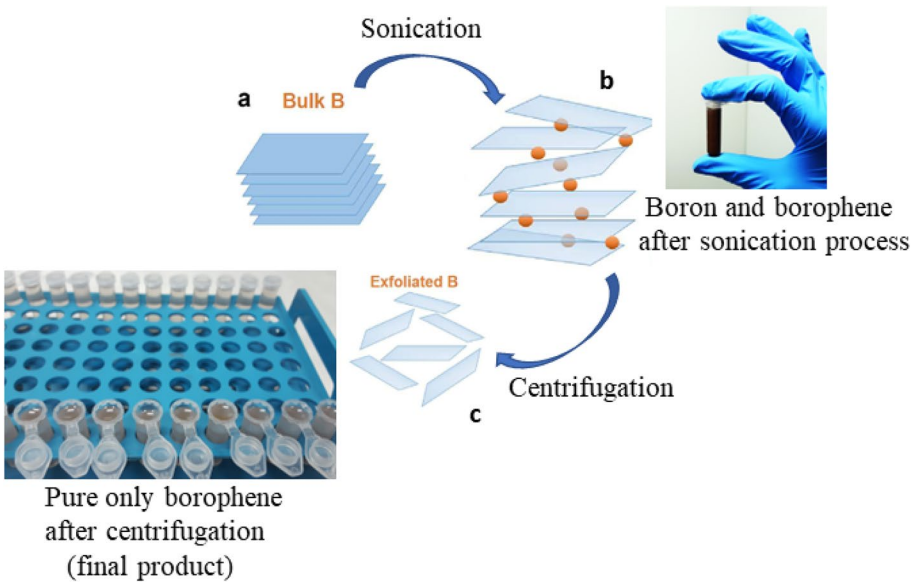


Fig. 1 Preparation stages of the exfoliated borophene [53–56]

2.2 Device fabrication

To prepare PANI:Borophene nanocomposites, 1-mg borophene and 1-mg PANI were added to 2-ml *N*-methyl-2-pyrrolidone solvent. The ingredients were mixed onto a magnetic stirrer for 5 min. Subsequently, the prepared solution was coated on cleaned p-type and n-type Si wafers. The wafers were cleaned via RCA procedure [57]. To prevent SiO_2 formation and impurities on the surface, they were dealt with HF:H_2O(1:10) solution. Aluminum Ohmic contact was formed at 10^{-6} Torr using physical vapor deposition. Spin coater was used to create a uniform PANI:Borophene interlayer at 1500 rpm. 150-nm Al and Au was coated onto the nanocomposite layer to create metallic contacts via physical vapor deposition [58–64]. Figure 2 shows the schematic diagram of fabricated Al/PANI:Borophene/p-Si and Au/PANI:Borophene/n-Si devices.

2.3 Characterization

Characterization of the borophene nanosheets was carried out using X-Ray Diffraction Spectroscopy (XRD, PAN analytical Xpert-Pro) and UV–Vis diffuse reflectance spectroscopy (Shimadzu UV-2501PC). Fytronix FY-7000 solar simulator measurement system was used to obtain *I–V* and *I–t* characteristics under different power intensities of light illumination. The surface characterization of prepared borophene and PANI:Borophene nanocomposite were fulfilled by High-Resolution Transmission Electron Microscopy (HRTEM) JEOL JEM-ARM200CFEG UHRTEM) and Scanning Electron Microscopy (SEM).

3 Results and discussion

The TEM images of the prepared borophene are depicted in Fig. 3. In the 50-nm scale image in Fig. 3a, exfoliated borophene nanosheets are seen free-standing in DMF. When a 20-nm scale image is taken by focusing on one of the borophene nanolayers, it is seen that the borophene nanolayer consists of hexagonal honeycomb structures with a regular morphology (Fig. 3b). When this borophene nanosheet was selected and FFT analysis was performed, it was proven that the crystal structure of borophene was hexagonal, as seen in Fig. 3c. When the selected borophene nanosheet was focused a little more with a microscope and 10-nm and 2-nm scale images were taken (Fig. 3d, e), it was proven that borophene had a hexagonal structure with a very smooth morphology.

Figure 4a shows the XRD analysis result of precursor boron and prepared borophene. Peaks related to the (003), (104), (021), and (324) planes of borophene have observed. These peaks prove that the prepared borophene is in the centrosymmetric β-rhombohedral phase (PDF31-0207 card).

Ultraviolet–visible (UV–Vis) diffuse reflectance spectroscopy has been conducted to determine the band gap energies. The Kubelka–Munk function method is applied to transform the collected data:

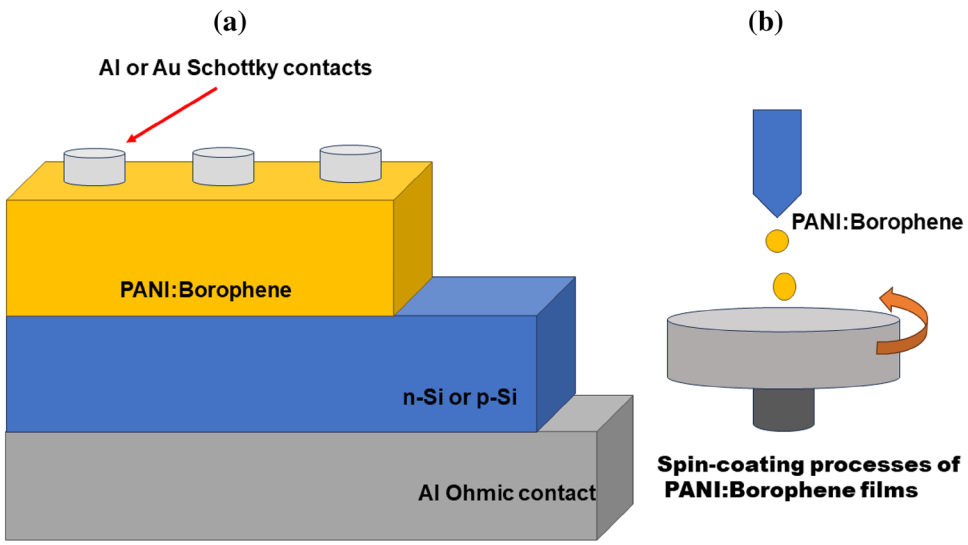


Fig. 2 **a** The schematic diagram of devices. **b** Spin-coating processes of PANI:Borophene films

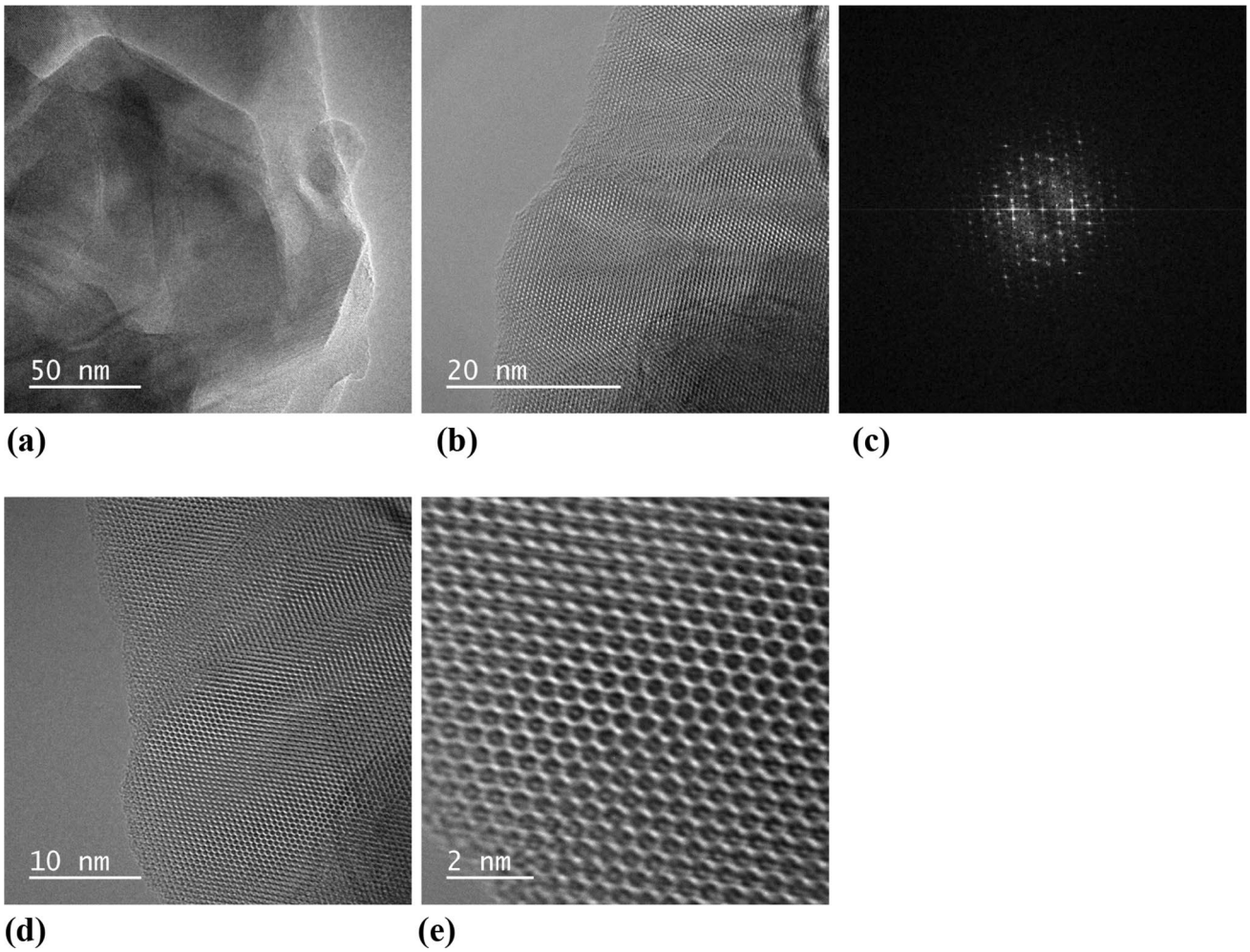


Fig. 3 The TEM analysis images for (**a**) 50 nm (**b**) 20 nm (**d**) 10 nm (**e**) 2nm and (**c**) the FFT pattern of the borophene [53–56]

$$F(R) = \frac{(1-R)^2}{2R}, \tag{1}$$

where R represents the diffuse reflectance value acquired from the diffuse reflectance measurements. The Tauc plot of the Kubelka–Munk function has been employed to estimate both direct and indirect band gap transitions of the prepared borophene as shown in Fig. 4b. The calculated band gap energies for the synthesized borophene have 0.94 eV and 1.74 eV for indirect and direct transition band gaps, respectively.

The SEM images of PANI and PANI:Borophene are given in Fig. 5, respectively. It can be seen from Fig. 5a that PANI thin film forms a smooth surface. The figure shows that PANI particles are nano-sized and the film is generally in agglomerated and uniform packages. The result of these uniform morphology and homogeneity provide an advantage for interfacial polymerization [65]. In Fig. 5b, a randomly grown PANI:borophene nano-shaped structure has observed. This PANI:Borophene nanocomposite thin film has created with fringes.

Figure 6 shows the typical semi-logarithmic current voltage (I–V) curves of the prepared structures Al/PANI:Borophene/p-Si and Au/PANI:Borophene/n-Si under dark and different light intensities (from 20 to 100 mW/cm^2). As can be seen from the figure, both structures exhibit a rectification attitude. It can be seen from Fig. 6 that the plots show a linear behavior in the middle parts of the forward bias region. However, as the forward voltage increases, it deviates from linearity due to the series resistance effect. On the other hand, the current value of Al/PANI:Borophene/p-Si at − 5 V is lower than the current values of Au/PANI:Borophene/n-Si structure and showed a weak voltage dependence under reverse bias. Whereas, a

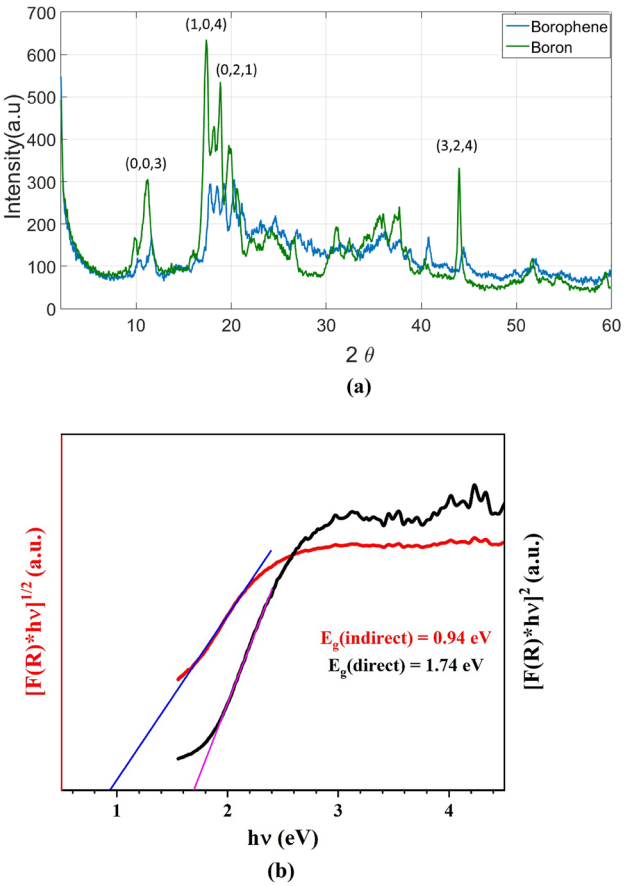


Fig. 4 **a** XRD analysis of the precursor boron and prepared borophene. **b** Tauc plots of the Kubelka–Munk function for the direct and indirect transitions of the prepared borophene

reverse bias has a negligible forward current, a forward bias has a significant forward current. A diode's depletion layer is significantly thicker in reverse bias and much thinner in forward bias. A diode's resistance increases with reverse bias and decreases with forward bias. Herein, we can easily observe the increase of the currents in forward bias and decrease of it in reverse current in both devices. For the light intensity of 100 mW/cm^2 at − 5 V in the reverse voltage region, the reverse current have been found 5.56×10^{-5} and 7.27×10^{-2} A for the structures Al/PANI:Borophene/p-Si and Au/PANI:Borophene/n-Si, respectively. This can be explained by the decrease in image force of the Schottky barrier height [64, 66].

In an ideal diode, the depletion region affects the forward bias current and this creates an exponential current–voltage correlation (Thermionic Emission Mechanism). The Thermionic Emission Mechanism is a dominant model, and it ignores other mechanisms. In this case it is possible to calculate the performance parameters such as diode's ideality factor (n), barrier height (Φ_B), and series resistance (R_s) using the thermionic correlation between current and voltage as follows [66]:

$$I = I_o\left[\exp\left(\frac{q(V - IR_s)}{nkT}\right) - 1\right]. \quad (2)$$

This model is used at the $V > 3kT/q$ voltage limit to remove contributions from reverse bias, where I_0 is the saturation current, n is the ideality factor, q is the electronic charge, V is the applied voltage, R_s is the series resistance, T is the temperature in Kelvin, and k is the Boltzmann constant. The linear regions of the semi-logarithmic I–V curves represent the current generated by the majority charge carriers using diffusion. On the other hand, the saturation current (I_0)

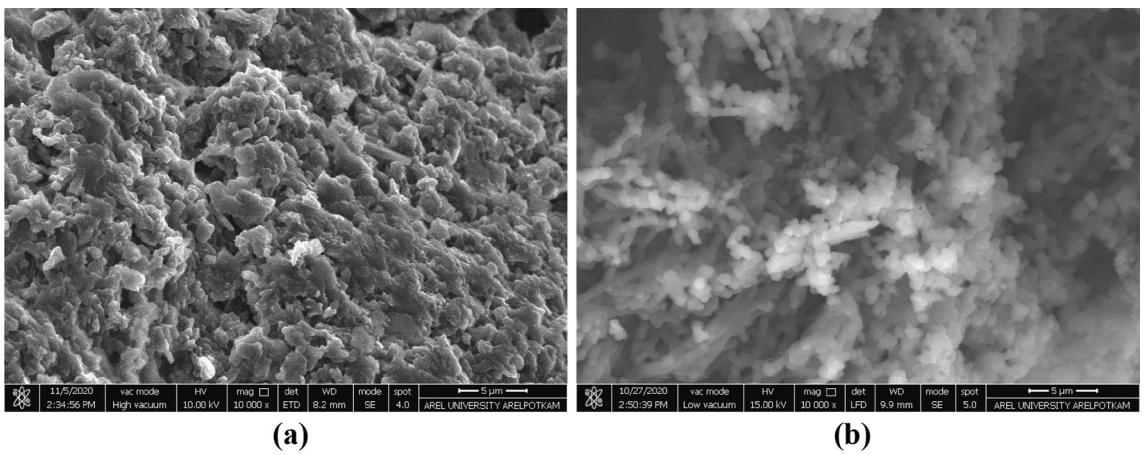


Fig. 5 SEM images of the **a** prepared PANI thin film and **b** prepared PANI:Borophene nanocomposite thin film

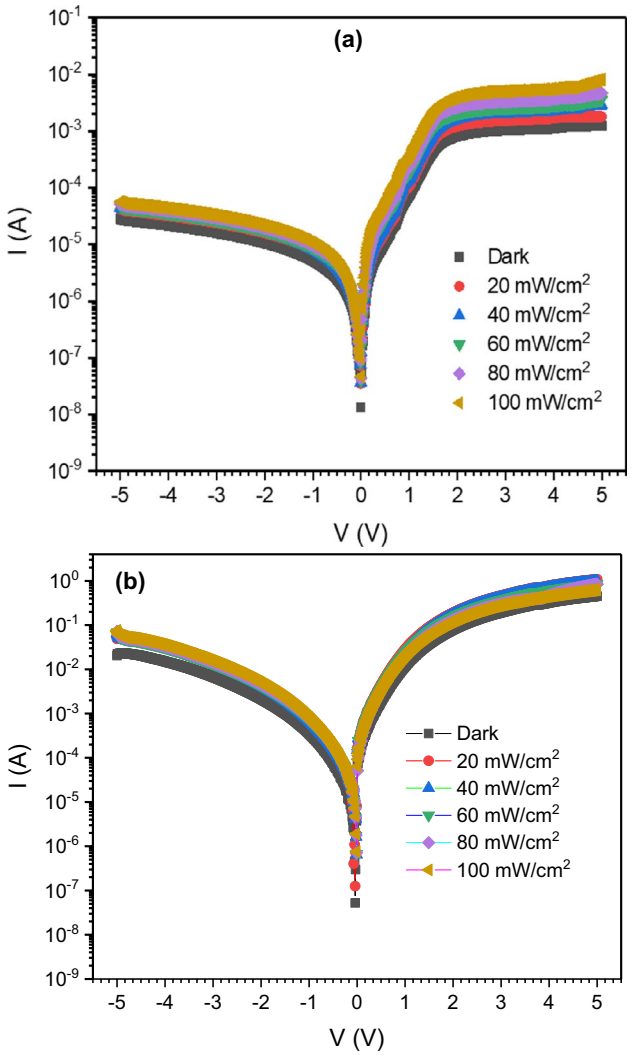


Fig. 6 Semi-logarithmic *I–V* characteristics of devices under different illumination and dark environment: **a** Al/PANI:Borophene/p-Si and **b** Au/PANI:Borophene/n-Si

created by minority charge carriers is given as follows [2, 67, 68]:

$$I_o = AA^*T^2\exp\left(-\frac{q}{kT}\Phi_B\right), \tag{3}$$

where A is the effective diode area, A^* is the effective Richardson constant (112 A/cm^2 K^2 for n-Si and 32 A/cm^2 K^2 for p-Si), and Φ_B is the barrier height. The I_0 values depending on the light intensity and dark environment obtained from the zero voltage point of linear region of semi-log *I–V* curves are tabulated in Table 1 for both structures. It can be seen from Fig. 6, the I_0 values of Au/PANI:Borophene/n-Si device is greater than the Al/PANI:Borophene/p-Si device.

Figure 7 shows the rectification ratios (*RR*) of Al/PANI:Borophene/p-Si and Au/PANI:Borophene/n-Si structures depending on light intensity. The ratio of forward current to the reverse current (at a specific voltage) is used to determine the *RR* value of diode. The *RR* values of the produced devices have been obtained at ± 5 V. As seen in Fig. 7b, the *RR* values for structure Au/PANI:Borophene/n-Si decrease with increasing light densities. This may be due to the possible contribution of charge carriers produced by photons to dark current and the increase of reverse voltage as a result of illumination [67, 68]. The *RR* has been found as 44.14 and 22.15 at ± 5 V under dark environment for devices Al/PANI:Borophene/p-Si and Au/PANI:Borophene/n-Si, respectively.

Figure 8 depicts the variation of ideality factor (n) and barrier height (Φ_B) as a function of illumination intensity. n values have been obtained using the tilt of linear region [Eq. (2)] of current–voltage plots. Φ_B values have been obtained with the help of Eq. (3). As seen from the figures, the n values of both devices are much larger than unity. The high n values obtained can be attributed to the presence of barrier inhomogeneities and series resistance [69, 70].

Table 1 Illumination-dependent electrical parameters of (a) Al/PANI:Borophene/p-Si and (b) Au/PANI:Borophene/n-Si devices

P (mW/cm^2)	PANI:Borophene/p-Si			PANI:Borophene/n-Si		
	n	I_o ($\times 10^{-7}$ A)	Φ_B (eV)	n	I_o ($\times 10^{-4}$ A)	Φ_B (eV)
Dark	2.27	1.44	0.667	3.96	0.714	0.506
20	2.21	2.04	0.658	3.92	1.55	0.486
40	2.35	3.06	0.648	4.21	1.65	0.485
60	2.49	4.26	0.639	4.28	1.41	0.489
80	2.60	4.75	0.636	4.49	1.30	0.491
100	2.75	10.1	0.617	4.50	1.23	0.492

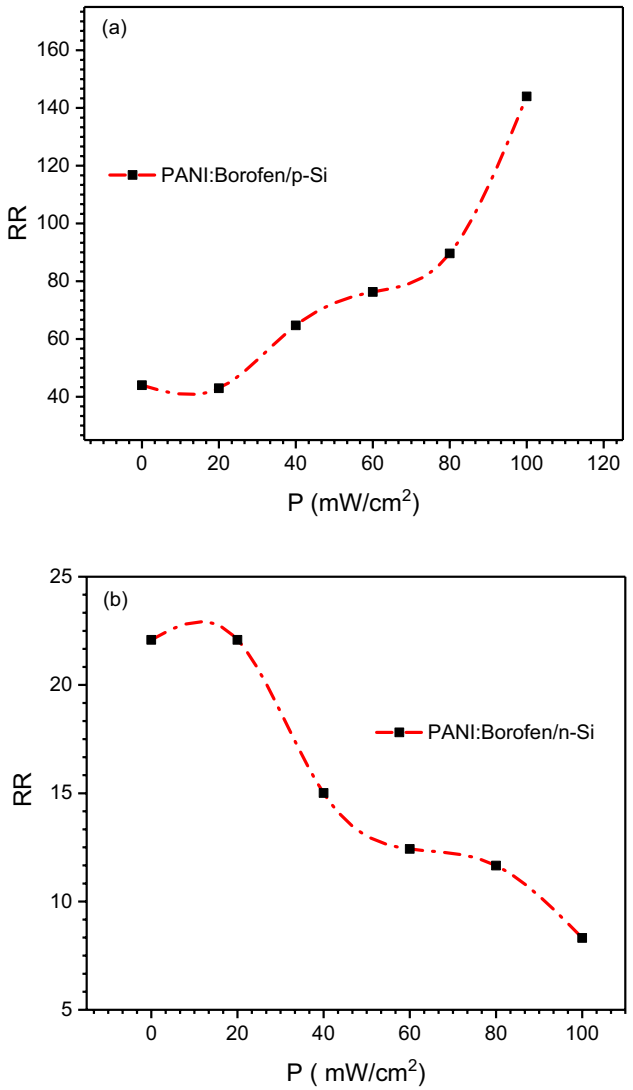


Fig. 7 The *RR* plots of devices under different illumination: **a** Al/PANI:Borophene/p-Si and **b** Au/PANI:Borophene/n-Si

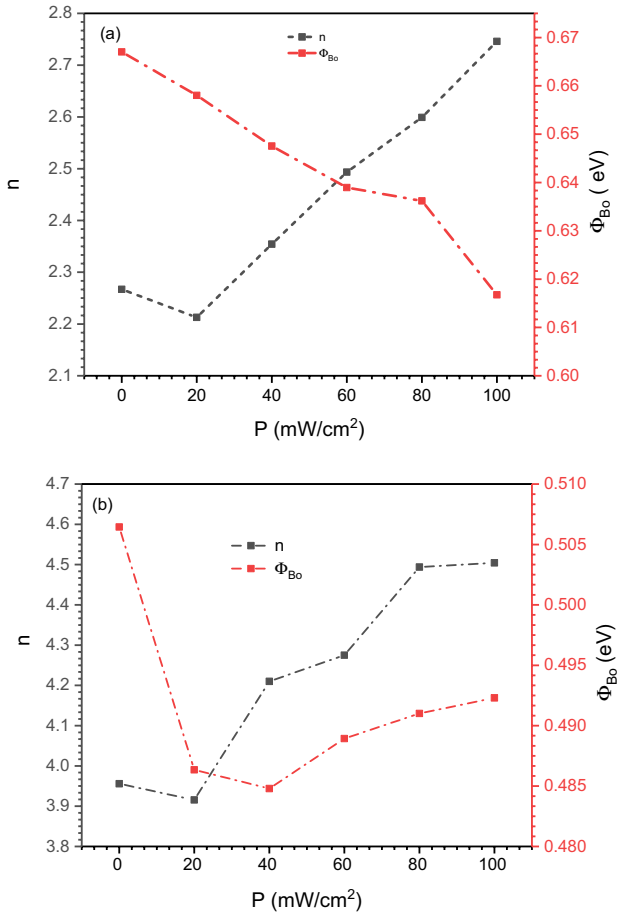


Fig. 8 *n* and Φ_B curves of devices under illumination: **a** Al/PANI:Borophene/p-Si and **b** Au/PANI:Borophene/n-Si

One of the reasons why the ideality factor is greater than unity is the generation-recombination currents that contribute to the thermionic emission mechanism of current. The increase in interface states as a result of possible defects creates inhomogeneity and this creates deviation from ideality. The *n* and Φ_B values for Al/PANI:Borophene/p-Si device have found to be 2.27 and 0.667 eV, respectively, in dark environment. Similarly, for device Au/PANI:Borophene/n-Si, these parameter values have been found to be 3.96 and 0.506 eV, respectively. The *n* and Φ_B values for devices Al/PANI:Borophene/p-Si and Au/PANI:Borophene/n-Si are listed in Table 1 as a function of light density. As seen from both figures, while the *n* values of the Al/PANI:Borophene/p-Si and the Au/PANI:Borophene/n-Si device started to decrease after a certain light intensity. This may be due to excess charged carriers produced under illumination. Moreover, the ratios of holes and electrons in the depletion region change under illumination. This causes the forward current in device to increase and, as a result, the ideality factor to decrease [71]. As seen in Fig. 8a and b, Φ_B increases with increasing light intensity. The increases in Φ_B can be attributed to the density of states present at the interface and the chemical reactions that occur. The increase in light density increased the mobility of charged carriers and, accordingly, the barrier height increased. Similar results have been reported by researchers [72, 73].

The exponential behavior of current–voltage curves is affected by series (R_s) and shunt (R_{sh}) resistance, and these parameters divert the curves from linear position when applied bias increases toward the forward

and reverse voltage regions [64, 66]. In order to high power and speed, the R_s value is expected to be low. However, the trap states and contact points within the device increase R_s value [74, 75]. Despite the series resistance value, the shunt resistance of the diode is expected to be quite high. However, due to the contacts within the device, current mechanisms affected by interface conditions and inhomogeneous surface, it may be associated with the leakage currents [76–78]. R_s and R_{sh} parameters are obtained from the junction resistance (R_j) of structure using the following expression [79].

$$R_j = \frac{\partial V}{\partial I}. \tag{4}$$

Figure 9a and b presents the R_s and R_{sh} curves of Al/PANI:Borophene/p-Si and Au/PANI:Borophene/n-Si devices at different light intensities. R_s and R_{sh} values have been found 2.7 Ω and 119.3 kΩ for Al/PANI:Borophene/p-Si at 20 mW/cm^2, respectively. At 100 mW/cm^2, these values have been obtained as 0.62 Ω and 88.63 kΩ, respectively.

Series resistance values of structures can also be determined by different methods such as the Cheung method as defined below [80–83].

$$\frac{dV}{d\ln I} = IR_s + n\left(\frac{kT}{q}\right) \tag{5}$$

and

$$H(I) = n\Phi_B + IR_s. \tag{6}$$

With this effective method, it is possible to determine n and Φ_B as well as calculating R_s. Figure 10a and b presents the dV/dln$I$ plots depending on I for devices

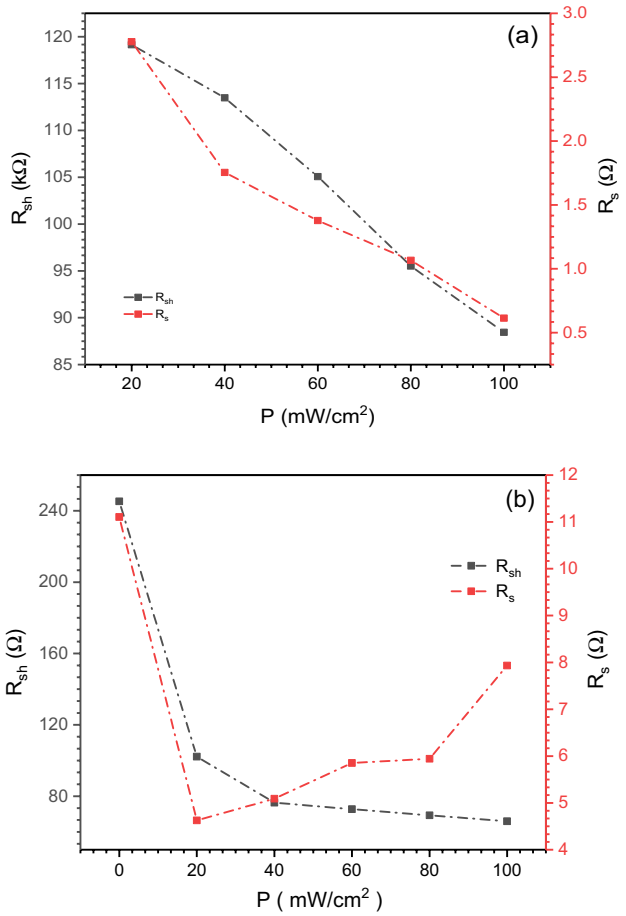


Fig. 9 R_s and R_{sh} curves of devices at different light intensities: **a** Al/PANI:Borophene/p-Si and **b** Au/PANI:Borophene/n-Si

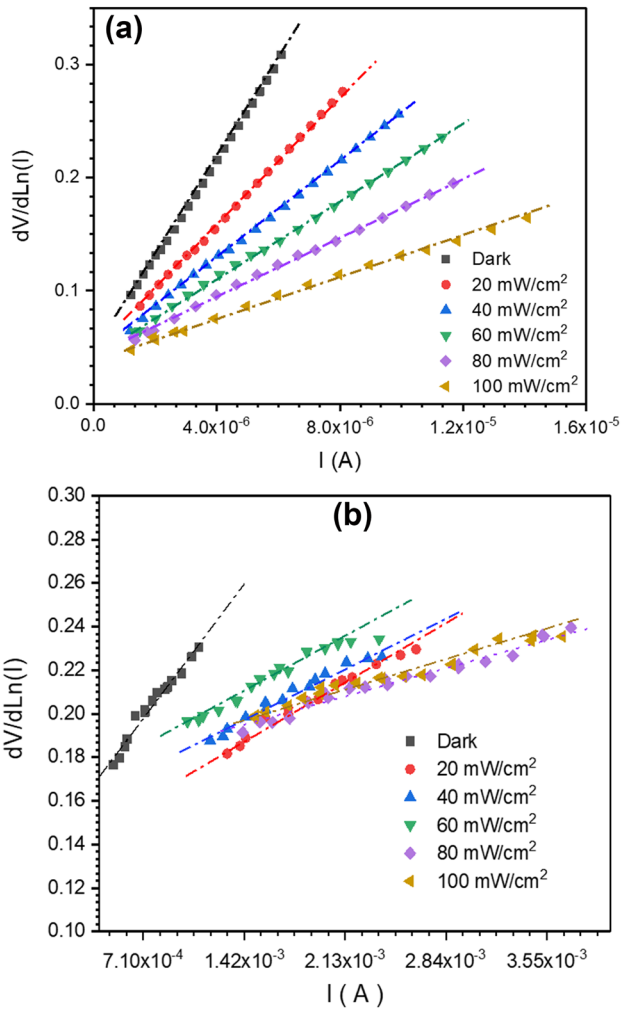


Fig. 10 The dV/dln$I$ vs. I plots at different illumination intensities: **a** Al/PANI:Borophene/p-Si and **b** Au/PANI:Borophene/n-Si

Al/PANI:Borophene/p-Si and Au/PANI:Borophene/n-Si at different light intensities. As can be seen from both figures, Eq. (5) gives a straight line in the area where there is bending in the high forward bias region of the *I–V* plots. The slope of this straight line gives R_s and the point where it intersects the *y*-axis gives nkT/q.

Figures 11a and b depicts the $H(I)$ plots depending on I of Al/PANI:Borophene/p-Si and Au/PANI:Borophene/n-Si devices at distinct light intensity. Each plot gives a straight line and $n\Phi_B$ is obtained from the point where it intersects the *y*-axis. The R_s values of Al/PANI:Borophene/p-Si and Au/PANI:Borophene/n-Si that obtained from the plots at different light densities according to Cheung method are listed in Table 2. It is seen from Table 2, the R_s values of Al/PANI:Borophene/p-Si and Au/PANI:Borophene/n-Si devices decreased with increasing light intensity. This may be caused by increased charge carriers at the interface as a result of increased

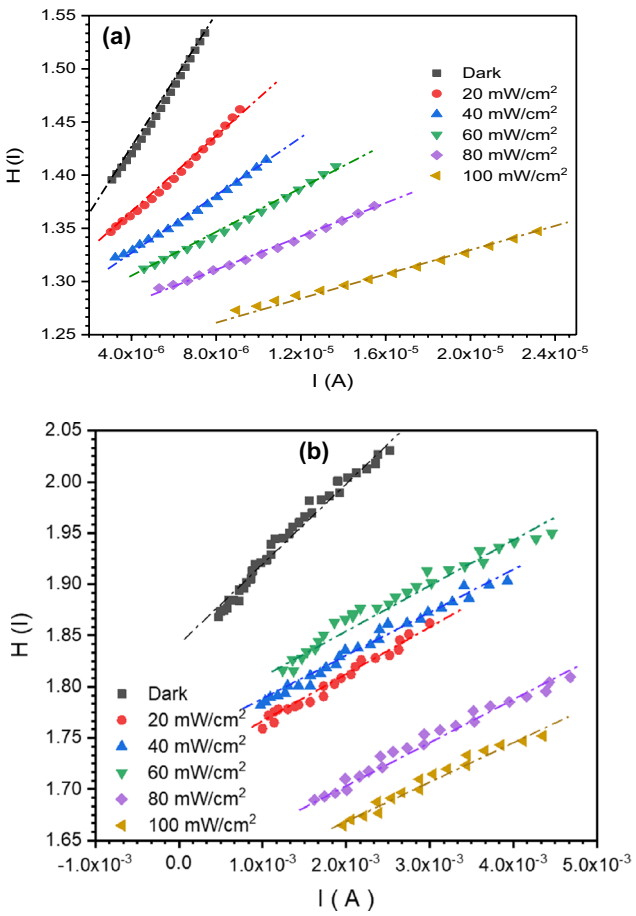


Fig. 11 The $H(I)$ vs. I plots at different illumination intensities: **a** Al/PANI:Borophene/p-Si and **b** Au/PANI:Borophene/n-Si

Table 2 Illumination dependent series resistance values of Al/PANI:Borophene/p-Si and Au/PANI:Borophene/n-Si devices according to Cheung method

P (mW/cm^2)	PANI:Borophene/p-Si		PANI:Borophene/n-Si	
	*R_s (Ω)	**R_s (Ω)	*R_s (Ω)	**R_s (Ω)
Dark	43.271	31.749	86	82
20	28.665	18.765	36	48
40	21.505	12.896	34	43
60	17.079	10.550	33	42
80	13.200	7.616	19	40
100	8.956	5.159	17	39

*dV/dln$I$

**$H(I)$

illumination [83]. Moreover, R_s values calculated with the help of Cheung functions are close to each other and decrease with increasing light intensity.

Figure 12 shows the light intensity dependence of R_s values and used Cheung functions. As seen in the calculations, the second R_s value obtained from the slope of the $H(I)$ function is also in agreement with the previous calculated value. The plots in Fig. 12 have been used to verify the consistency of the Cheung approach.

Photocurrent structures of diodes can be analyzed with the following expression depending on light intensity and photocurrent [84, 85].

$$I_{ph} = AP^m, \tag{7}$$

where I_{ph} is the photocurrent caused by illumination intensity, P is the applied illumination density, m is the illumination constant, and A is the constant of proportionality between photocurrent and light intensity. In Fig. 13, the plots of $\log(I_{ph}) - \log(P)$ of Al/PANI:Borophene/p-Si and Au/PANI:Borophene/n-Si devices are presented. As can be seen from Fig. 13a and b, a linear behavior has obtained for both devices. This shows that the diodes have a linear photoconductivity property. Accordingly, it is possible to determine the photoconductivity mechanisms in devices with the m value [86]. This process depends on the lifetime of the photo-carriers and is carried out in three different ways. When $m = 1$, the photoconductivity mechanism of device is under the effect of monomolecular recombination. As m values increase, it is possible to talk about low density or unoccupied trap levels. The m values obtained from the linear curves in Fig. 13a and b are 0.44 and 0.33 for structures Al/

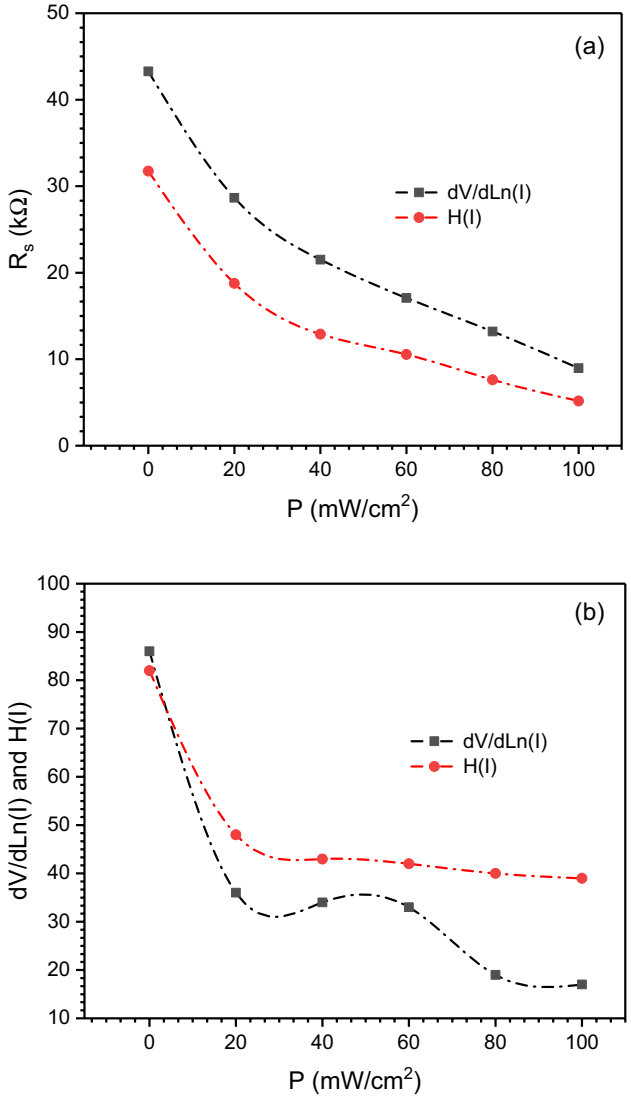


Fig. 12 The calculated R_s (**a**) and Cheung functions (**b**) plots depending on illumination intensities

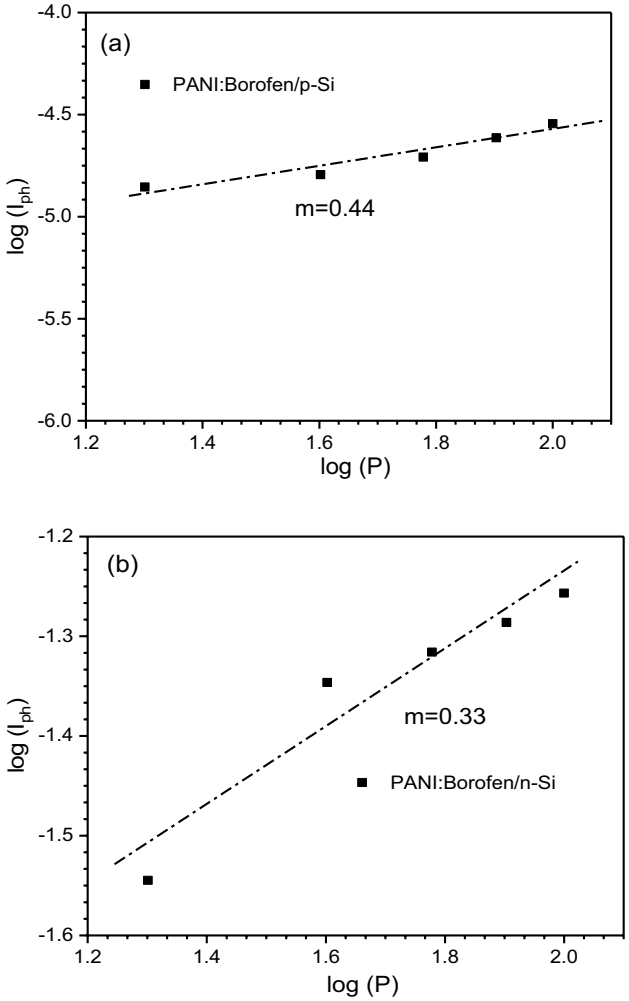


Fig. 13 log (I_{ph}) − log(P) plots: **a** Al/PANI:Borophene/p-Si and **b** Au/PANI:Borophene/n-Si

PANI:Borophene/p-Si and Au/PANI:Borophene/n-Si, respectively. These values are in the $0 < m < 1$ range and indicate the existence of permanent localized states inside device [68, 78, 85, 86]. For device Al/PANI:Borophene/p-Si (in Fig. 13a), it can be seen that the photocurrent increases from 1.40×10^{-5} to 2.85×10^{-5} A with increasing light intensity. Similarly, for device Au/PANI:Borophene/n-Si (in Fig. 13b), it is seen that the photocurrent increases from 2.85×10^{-2} to 5.54×10^{-2} A with increasing light intensity. This situation shows that the electrons in valence band jump toward the conduction band with light energy they gained [87–90]. The photocurrent values at different light densities are listed in Table 3 for both devices.

The responsivity (R) and sensitivity (K) are characteristic parameters of a photodiode and are given by the following expressions [88–92].

$$R = \frac{I_{ph} - I_d}{P_{in}}, \tag{8}$$

$$K = \frac{I_{ph} - I_d}{I_d}, \tag{9}$$

where I_{Ph} is the photocurrent under light intensity, P_{in} is the incident light density, and I_d is the dark current. In Fig. 14a and b, the R and K plot of Al/PANI:Borophene/p-Si and Au/PANI:Borophene/n-Si devices are illustrated. For device Au/PANI:Borophene/n-Si, the R value has been found to be 70.79 A/W under the light density of 100 mW/

Table 3 Various detector parameters of the Al/PANI:Borophene/p-Si and Au/PANI:Borophene/n-Si photodiode for various power

P (mW/cm^2)	PANI:Borophene/p-Si				PANI:Borophene/n-Si			
	I_{ph} ($\times 10^{-5}$ A)	K (A/cm^2)	R (A/W)	D ($\times 10^9$ Jones)	I_{ph} ($\times 10^{-5}$ A)	K (A/cm^2)	R (A/W)	D ($\times 10^{11}$ Jones)
20	1.40	0.499	0.089	2.63	2.85	1.40	181.70	1.99
40	1.61	0.574	0.051	1.51	4.51	2.21	143.48	1.57
60	1.96	0.699	0.042	1.23	4.83	2.37	102.60	1.13
80	2.43	0.869	0.039	1.15	5.18	2.54	82.42	0.90
100	2.85	1.019	0.036	1.08	5.54	2.71	70.54	0.77

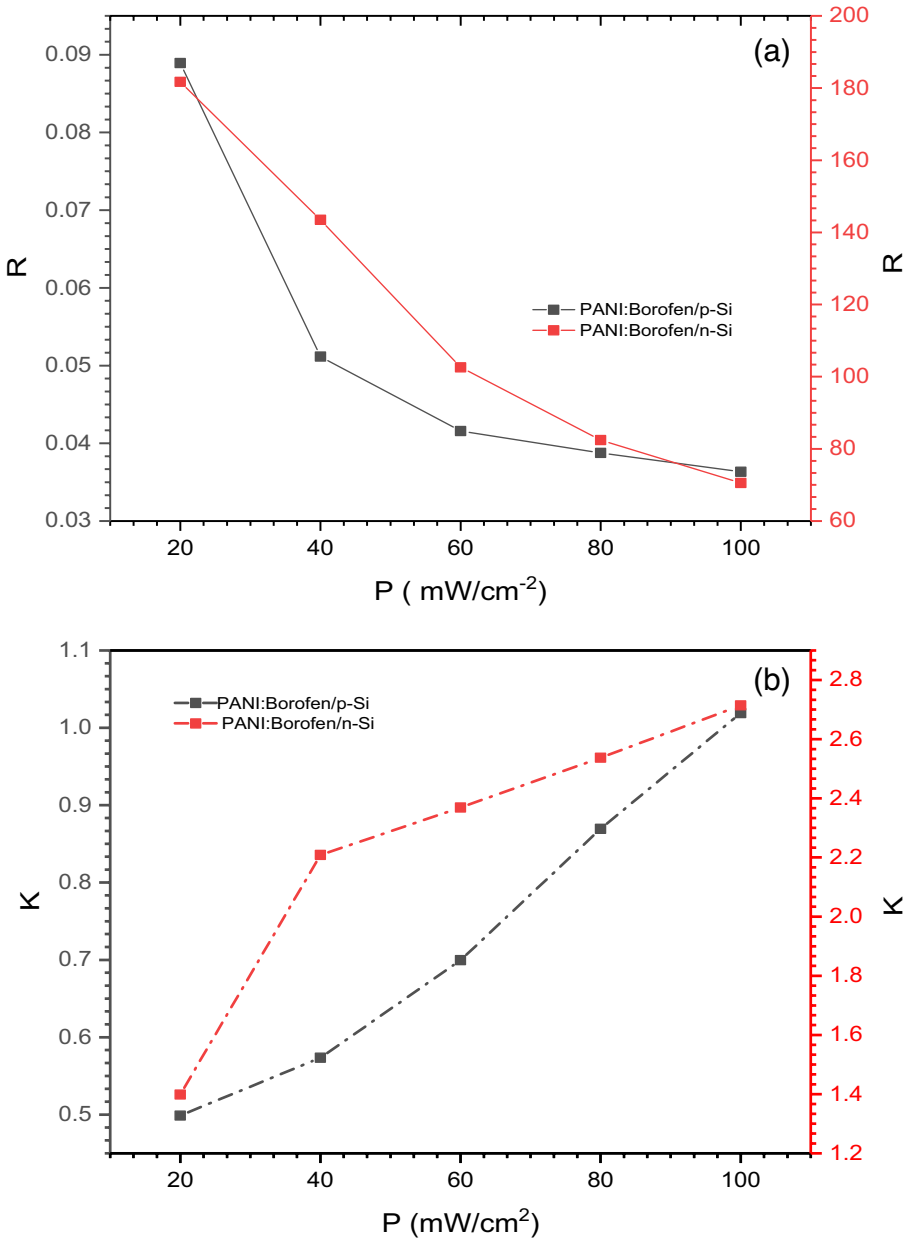


Fig. 14 **a** R and **b** K plot with light intensity

cm^2 at − 5 V spot voltage. Similarly, for device Au/PANI:Borophene/p-Si, the R value has been found to be 3.61×10^{-2} A/W. The responsivity for Au/PANI:Borophene/n-Si device at 100 mW/cm^2 is 2.98 times higher than that of Co/p-Si/Al photodiode with Congo Red interfacial layer [91] and 18.05 times higher than the photodiode with the copper complex interfacial layer [92]. The K values of Al/PANI:Borophene/p-Si device have found to be 2.68 A/cm^2 under 100-mW/cm^2 illumination. The sensitivity of Al/PANI:Borophene/p-Si device is 2.31 times higher than that of photodiode with Congo Red interfacial layer [91]. These results show that the fabricated device has a good photo-sensing property. From these results, it can be seen that the devices produced have good photo-sensing ability. The R and K values of Al/PANI:Borophene/p-Si and Au/PANI:Borophene/n-Si that are obtained at various light densities are tabulated in Table 3.

One of the characteristic parameters of photodiodes is detectivity (D). This parameter determines the diode's ability to detect low optical signals and is expressed with the following formulation [93]:

$$D = \frac{R\sqrt{A}}{\sqrt{2qI_d}}, \tag{10}$$

where R and I_d are the photoresponsivity and dark current, respectively, A is the effective area where incidental light is absorbed, and q is the electronic charge. Light intensity-dependent detectivity for devices Al/PANI:Borophene/p-Si and Au/PANI:Borophene/n-Si is given in Fig. 15. As can be seen from the figure, the detectivity of both devices decreases with increasing light intensity. This decrease in detectivity may be attributed to traps present at the heterojunction interface [94]. The maximum detectivity under 5 V bias and at 20 mW/cm^2 light intensity has been found to be 1.99×10^{11} Jones for the Au/PANI:Borophene/n-Si sample. As can be seen, a high level of detectivity has been obtained under low intensity illumination. This shows that the manufactured devices are very sensitive to low optical power.

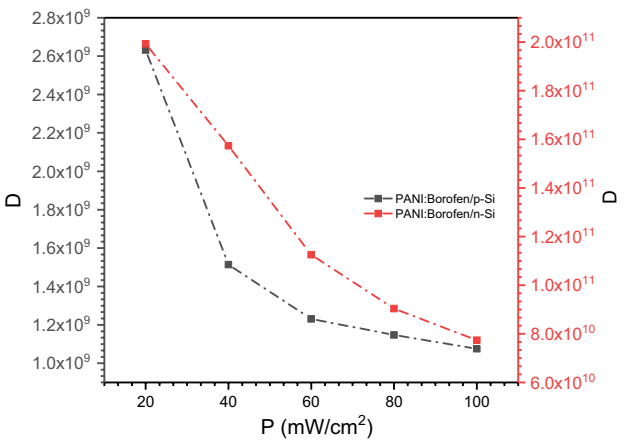


Fig. 15 D plots depending on illumination intensities

For a more detailed photoconductivity examination, the time-dependent transient measurement method has been used. These measurements are a frequently used technique to understand the photoconductivity mechanism of a device for different optical power densities and to see the photoresponse properties during on–off states [95, 96]. Figure 16a and b displays the transient plots of Al/PANI:Borophene/p-Si and Au/PANI:Borophene/n-Si devices at − 5 V bias depending on the light intensity. When illumination is turned on, the number of free charge carriers increases and contributes to the flowing current. Thus, the photocurrent level quickly reaches saturation. When illumination is turned off, charge carriers drop to low levels and the current photocurrent quickly drops to the initial level [97]. Thus, a reverse switching behavior begins. As can be seen from the figures, the photoresponds of both produced devices are highly repeatable. As seen in Fig. 16a, b, the produced devices showed a fast photoresponse and good stability at different light intensities and reached the maximum photocurrent level in approximately 1 s. For sample Al/PANI:Borophene/p-Si, it increased from 5.78×10^{-4} to 2.26×10^{-3} A at an illumination intensity of 100 mW/cm^2 and decreased to 6×10^{-5} A when the illumination has turned off. Similarly, for sample Au/PANI:Borophene/n-Si, these values increase from 1.8×10^{-4} to 7.54×10^{-4} A and decrease 2.48×10^{-5} A. These results clearly show that the produced devices exhibit photoconductive behaviors. This initial rise in photocurrent when illumination begins provides information about the production mechanisms of free charge carriers. The decrease in current when the lighting is turned off is a symptom of the trapping mechanisms of charge carriers at deep levels. This occurs as a result of the layered surface properties of the device [98].

Finally, the PANI:Borophene/Si Schottky diodes have been tested for salt (NaCl) detection. This salt detection experiment has carried out with different concentrations of salt solution (0–50 mM)

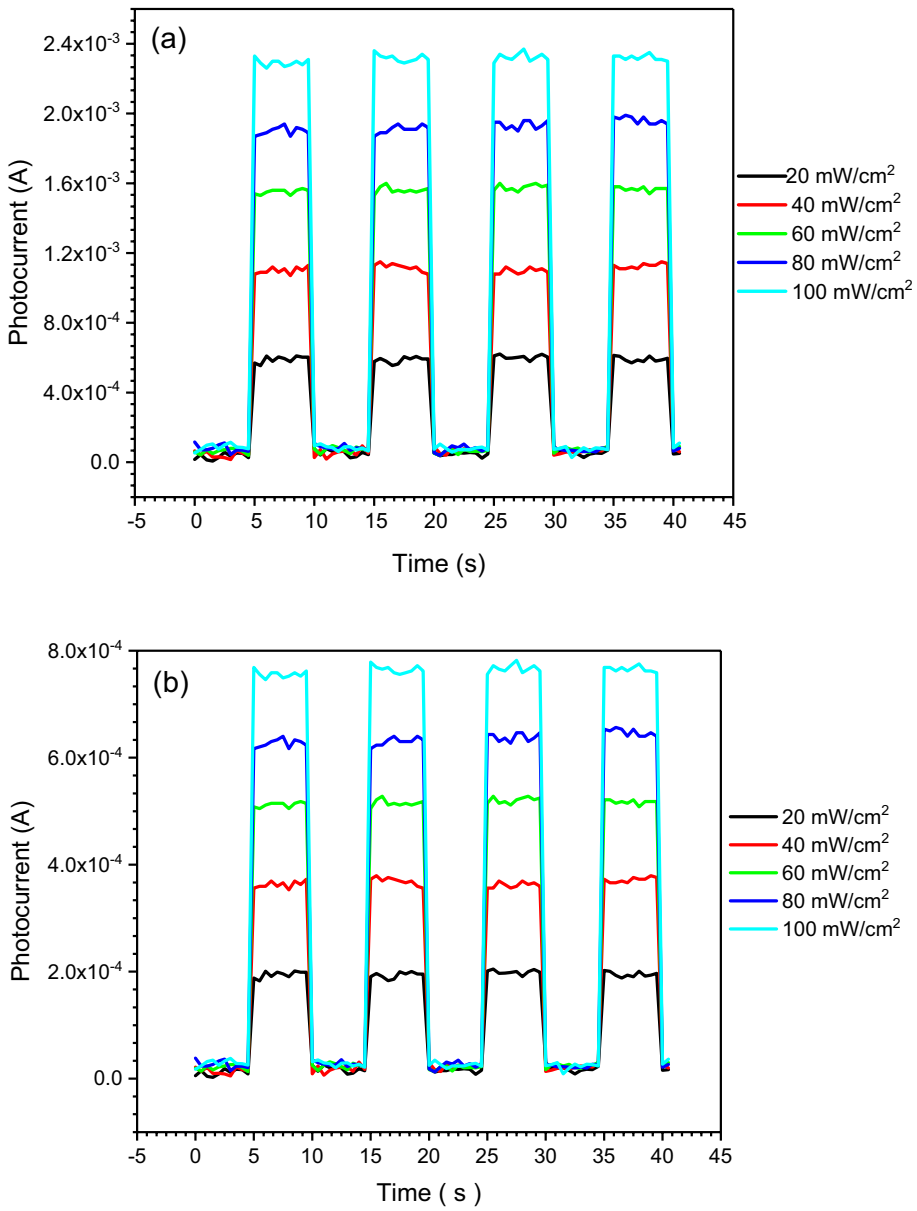


Fig. 16 The time-dependent transient plots under illumination intensity. **a** Al/PANI:Borophene/p-Si and **b** Au/PANI:Borophene/n-Si

deposited on the Al/PANI:Borophene/p-Si and the Au/PANI:Borophene/n-Si of the Schottky diode sensor and only, the Al/PANI:Borophene/p-Si diode response to salt solution concentration. The current–voltage plot under salt solution concentration at a range between + 5 and − 5 V for Al/PANI:Borophene/p-Si device is shown in Fig. 17. As seen in this figure, the average knee and the average breakdown voltage have obtained 3 V and − 4.6 V, respectively. Also, the current has increased with increasing salt solution concentration after the knee voltage of this diode. These increases in current are a result of the diode's series resistance (R_s) to current under salt concentrations (0–50 mM). The salt solution concentration-dependent current and the salt solution concentration-dependent series resistance plots for Al/PANI:Borophene/p-Si diode are given in Fig. 18. As seen in Fig. 18, firstly, a minimal decrease in the current has observed with 10-mM salt solution concentration applied to the diode and then an increase in the current has observed according to the increasing salt solution concentration (Fig. 18a).

On the other hand, as can be seen Fig. 18b, firstly, a minimal increase in the R_s of Al/PANI:Borophene/p-Si diode has observed with 10-mM salt solution concentration applied to the diode and then an decrease in

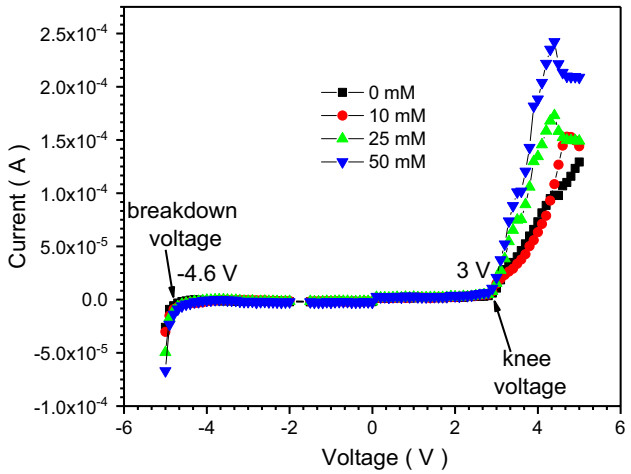


Fig. 17 The current–voltage plot under salt solution concentration for Al/PANI:Borophene/p-Si diode

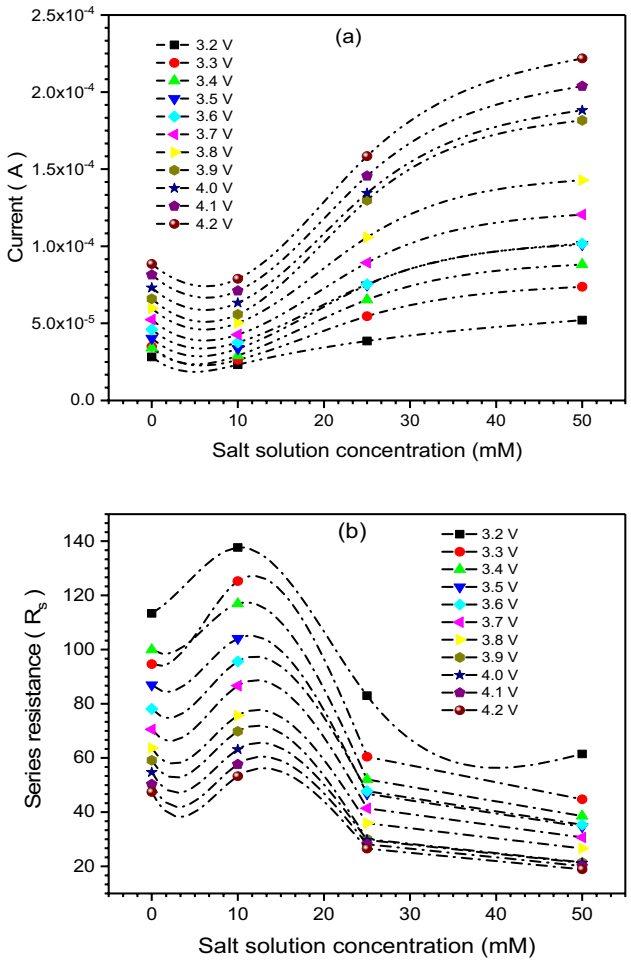


Fig. 18 **a** The salt solution concentration-dependent current and **b** the salt solution concentration-dependent series resistance plots for Al/PANI:Borophene/p-Si diode

the R_s of Al/PANI:Borophene/p-Si diode has observed according to the increasing salt solution concentration. Then, we investigated the time-dependent transient plots under salt solution concentration for Al/PANI:Borophene/p-Si diode (Fig. 19). This device has showed a fast salt concentration detection and good stability at different salt concentration changes. As a result, the Al/PANI:Borophene/p-Si diode is more sensitive salt concentration detection after knee voltage. From these results, it can be concluded that this diode has the characteristics of salt concentration detection sensor and it successfully detected salt concentration changes with respect to current flow [99–101].

4 Conclusion

In this study, a Schottky structure consisting of a PANI:Borophene/Si interface, which has not been reported before in the literature, has been fabricated and its photodiode properties have been investigated under different light intensities. It has been observed that the structures exhibit photoconductive behavior from *I–V* characteristics depending on illumination. The devices showed rectification features at all illumination intensities. Time-dependent photoconductivity measurements have shown that the photocurrent amounts of the devices depend on the light intensity, and the maximum photocurrent has reached in approximately one second. When the characteristic photodiode parameters have been

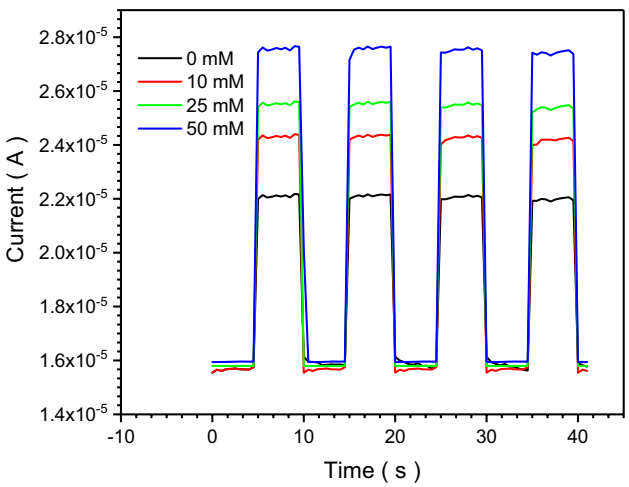


Fig. 19 The time-dependent transient plots under salt solution concentration for Al/PANI:Borophene/p-Si diode

examined, it has been seen that the structures had good photo-detection ability. It has been observed that it exhibits a very good response and quite high detectivity behavior to measurements at low light intensity. This shows that the produced devices may be candidates for opto-electronic applications such as a photodiode and photosensor. Finally, the PANI:Borophene/Si Schottky diodes have been tested for NaCl detection. Only, the Al/PANI:Borophene/p-Si diode response to salt solution concentration and this diode has the characteristics of salt concentration detection sensor and it successfully detected salt concentration changes with respect to current flow. This work will continue with trials of organic compounds/metabolite detection for possible biosensing applications for cheaper and volume fabrication in low-income countries.

Acknowledgements

The authors gratefully acknowledge the Scientific and Technological Research Council of Turkey (TUBITAK) due to the financial support for the Project 122N962, and Hitit University of BAP due to the financial support for the Project FEF19004.15.010, FEF19002.15.001, FEF01.13.003.

Author contributions

DEY contributed to investigation, methodology, writing, reviewing, & editing of the manuscript, funding, and supervision. SK contributed to investigation, methodology, and writing, reviewing, & editing of the manuscript. MY contributed to investigation, methodology, writing, reviewing, & editing of the manuscript, and funding. NT contributed to methodology, writing and reviewing of the manuscript, and funding. AG contributed to investigation and methodology. BBA contributed to investigation and methodology. MY contributed to methodology, writing, reviewing, & editing of the manuscript, and supervision.

Funding

Open access funding provided by the Scientific and Technological Research Council of Türkiye (TÜBİTAK). The authors have not disclosed any funding.

Data availability

The datasets generated during and/or analyzed during the current study are available from the corresponding author upon reasonable request.

Declarations

Competing interests The authors declare that they have no known competing financial interests or personal relationships that could have appeared to influence the work reported in this paper.

Open Access This article is licensed under a Creative Commons Attribution 4.0 International License, which permits use, sharing, adaptation, distribution and reproduction in any medium or format, as long as you give appropriate credit to the original author(s) and the source, provide a link to the Creative Commons licence, and indicate if changes were made. The images or other third party material in this article are included in the article's Creative Commons licence, unless indicated otherwise in a credit line to the material. If material is not included in the article's Creative Commons licence and your intended use is not permitted by statutory regulation or exceeds the permitted use, you will need to obtain permission directly from the copyright holder. To view a copy of this licence, visit http://creativecommons.org/licenses/by/4.0/.

References

1. M. Soylu, O.A. Al-Hartomy, S.A.F. Al Said, A.A. Al-Ghamdi, I.S. Yahia, F. Yakuphanoglu, Controlling of conduction mechanism and electronic parameters of silicon–metal junction by mixed Methylene Blue/2′-7′-dichlorofluorescein. Microelectron. Reliab. **53**, 1901–1906 (2013). https://doi.org/10.1016/j.microrel.2013.05.008
2. E.H. Rhoderick, R.H. Williams, *Metal Semiconductor Contacts* (Cleredon Press, Oxford, 1988)
3. S.M. Sze, K.K. Ng, *Physics of Semiconductor Devices* (Wiley, Hoboken, 2007)
4. S.S. Li, *Semiconductor Physical Electronics* (Springer, New York, 2006)

5. Q. He, M. Worku, H. Liu, E. Lochner, A.J. Robb, S. Lteif, J.S.R.V. Winfred, K. Hanson, J.B. Schlenoff, B.J. Kim, B. Ma, Highly efficient and stable perovskite solar cells enabled by low-cost industrial organic pigment coating. Angew. Chem. Int. Ed. **60**(5), 2485–2492 (2021)
6. J. Song, L. Zhu, C. Li, J. Xu, H. Wu, X. Zhang, Y. Zhang, Z. Tang, F. Liu, Y. Sun, High-efficiency organic solar cells with low voltage loss induced by solvent additive strategy. Matter **4**(7), 2542–2552 (2021)
7. B.D. Choudhury, C. Lin, S.M.A.Z. Shawon, J.S. Martinez, J. Gutierrez, M.N. Huda, F. Cesano, K. Lozano, J.Z. Zhang, M.J. Uddin, Carbon fibers coated with ternary Ni-Co-Se alloy particles as a low-cost counter electrode for flexible dye sensitized solar cells. ACS Appl. Energy Mater. **4**, 870–878 (2021)
8. A. Srivastava, D. Sharma, P. Kumari, M. Dutta, S.K. Srivastava, Highly efficient PEDOT:PSS/silicon hybrid solar cells via effective surface microengineering of low-cost solar-grade silicon wafers. ACS Appl. Energy Mater. **4**(4), 4181–4198 (2021)
9. S.H. Kim, S.H. Park, K. Lee, Efficiency enhancement in polymer optoelectronic devices by introducing titanium sub-oxide layer. Curr. Appl. Phys. **10**(3), S528–S531 (2010)
10. M.A. Green, Y. Hishikawa, E.D. Dunlop, D.H. Levi, J. Hohl-Ebinger, M. Yoshita, A.W.Y. Ho-Baillie, Solar cell efficiency tables (version 53). Prog. Photovolt. Res. Appl. **27**, 3–12 (2019)
11. B.A. Gozeh, A. Karabulut, C.B. Ismael, S.I. Saleh, F. Yakuphanoglu, Zn-doped CdO effects on the optical, electrical and photoresponse properties of heterojunctions-based photodiodes. J. Alloys Compd. **872**, 159624 (2021)
12. H.G. Çetinkaya, H. Tecimer, H. Uslu, S. Altındal, Photovoltaic characteristics of Au/PVA (Bi-doped)/n-Si Schottky barrier diodes (SBDs) at various temperatures. Curr. Appl. Phys. **13**, 1150–1156 (2013)
13. D.Y. Zhang, C.W. Ge, J.Z. Wang, T.F. Zhang, Y.C. Wu, F.X. Liang, Single-layer graphene-TiO_2 nanotubes array heterojunction for ultraviolet photodetector application. Appl. Surf. Sci. **387**, 1162–1168 (2016)
14. W.Y. Kong, G.A. Wu, K.Y. Wang, T.F. Zhang, Y.F. Zou, D.D. Wang, L.B. Luo, Graphene-β-Ga_2O_3 heterojunction for highly sensitive deep UV photodetector application. Adv. Mater. **28**, 10725–10731 (2016)
15. Z.Y. Hai, M.K. Akbari, C.Y. Xue, H.Y. Xu, L. Hyde, S. Zhuiykov, Wafer-scaled monolayer WO_3 windows ultra-sensitive, extremely-fast and stable UV-A photodetection. Appl. Surf. Sci. **405**, 169–177 (2017)
16. X.H. Zhang, S.J. Chua, A.M. Yong, H.Y. Yang, S.P. Lau, S.F. Yu, X.W. Sun, L. Miao, M. Tanemura, S. Tanemura, Exciton radiative lifetime in ZnO nanorods fabricated by vapor phase transport method. Appl. Phys. Lett. **90**, 013107 (2007)
17. Y. Danhara, T. Hirai, Y. Harada, N. Ohno, Exciton luminescence of ZnO fine particles. Phys. Status Solidi (c) **3**, 3565–3568 (2006)
18. J.H. Lim, C.K. Kang, K.K. Kim, I.K. Park, D.K. Hwang, S.J. Park, UV electroluminescence emission from ZnO light-emitting diodes grown by high-temperature radiofrequency sputtering. Adv. Mater. **18**, 2720–2724 (2006)
19. S. Aydogan, M. Saglam, A. Turut, On the barrier in homogeneities of polyaniline/p-Si/Al structure at low temperature. Appl. Surf. Sci. **250**(1), 43–49 (2005)
20. M. Wolszczak, J. Kroh, M.M.A. Hamid, Some aspects of the radiation processing of conducting polymers. Radiat. Phys. Chem. **45**(1), 71–78 (1995)
21. G. Gustafsson, G.M. Treacy, Y. Cao, F. Klavetter, N. Colaneri, A.J. Heeger, The plastic led: a flexible light-emitting device using a polyaniline transparent electrode. Synth. Met. **57**(1), 4123–4127 (1993)
22. K. Watanabe, T. Taniguchi, H. Kanda, Direct bandgap properties and evidence for ultraviolet lasing of hexagonal boron nitride single crystal. Nat. Mater. **3**(6), 404 (2004)
23. G. Liu, X.L. Lei, M.S. Wu, B. Xu, C.Y. Ouyang, Comparison of the stability of free-standing silicene and hydrogenated silicene in oxygen: a first principles investigation. J. Phys.: Condens. Matter **26**(35), 355007 (2014)
24. A. Molle, C. Grazianetti, L. Tao, D. Taneja, M.H. Alam, D. Akinwande, Silicene, silicene derivatives, and their device applications. Chem. Soc. Rev. **47**(16), 6370 (2018)
25. G. Li, L. Zhang, W. Xu, J. Pan, S. Song, Y. Zhang, H. Zhou, Y. Wang, L. Bao, Y.Y. Zhang, S. Du, M. Ouyang, S.T. Pantelides, H.J. Gao, Stable silicone in graphene/silicene van der Waals heterostructures. Adv. Mater. **30**(49), 1804650 (2018)
26. G. Liu, S.B. Liu, B. Xu, C.Y. Ouyang, H.Y. Song, S. Guan, S.A. Yang, Multiple Dirac points and hydrogenation-induced magnetism of germanene layer on Al(111) surface. J. Phys. Chem. Lett. **6**(24), 4936 (2015)
27. X.R. Hu, J.M. Zheng, Z.Y. Ren, Strong interlayer coupling in phosphorene/graphene van der Waals heterostructure: a first-principles investigation. Front. Phys. **13**, 137302 (2017)
28. S. Zhang, Z. Yan, Y. Li, Z. Chen, H. Zeng, Atomically thin arsenene and antimonene: semimetal-semiconductor and indirect-direct band-gap transitions. Angew. Chem. Int. Ed. **54**(10), 3112 (2015)
29. J. Ji, X. Song, J. Liu, Z. Yan, C. Huo, S. Zhang, M. Su, L. Liao, W. Wang, Z. Ni, Y. Hao, H. Zeng, Two-dimensional antimonene single crystals grown by van der Waals epitaxy. Nat. Commun. **7**(1), 13352 (2016)
30. Z.-Q. Wang, T.Y. Lü, H.Q. Wang, Y.P. Feng, J.C. Zheng, Review of borophene and its potential applications. Front. Phys. **14**(3), 33403 (2019)
31. E.S. Penev, A. Kutana, B.I. Yakobson, Can twodimensional boron superconduct? Nano Lett. **16**(4), 2522 (2016)
32. A. Lopez-Bezanilla, P.B. Littlewood, Electronic properties of 8–Pmmn borophene. Phys. Rev. B **93**, 241405(R) (2016)
33. B. Peng, H. Zhang, H.Z. Shao, Y.F. Xu, R.J. Zhang, H.Y. Zhu, Electronic, optical, and thermodynamic properties of borophene from first-principle calculations. J. Mater. Chem. C **4**(16), 3592 (2016)
34. R.C. Xiao, D.F. Shao, W.J. Lu, H.Y. Lv, J.Y. Li, Y.P. Sun, Enhanced superconductivity by strain and carrier-doping in borophene: a first principles prediction. Appl. Phys. Lett. **109**(12), 122604 (2016)
35. X.B. Yang, Y. Ding, J. Ni, Ab initio prediction of stable boron sheets and boron nanotubes: structure, stability, and electronic properties. Phys. Rev. B **77**, 041402(R) (2008)
36. H. Liu, J. Gao, J. Zhao, From boron cluster to two-dimensional boron sheet on Cu(111) surface: growth mechanism and hole formation. Sci. Rep. **3**(1), 3238 (2013)
37. V. Wang, W.T. Geng, Lattice defects and the mechanical anisotropy of borophene. J. Phys. Chem. C **121**(18), 10224 (2017)
38. H. Cui, X. Zhang, D. Chen, Borophene: a promising adsorbent material with strong ability and capacity for SO_2 adsorption. Appl. Phys. A **124**, 636 (2018)
39. T. Sohail, J.D. Zika, D.B. Irving, J.A. Church, Observed poleward freshwater transport since 1970. Nature **602**, 617–622 (2022)
40. H. Kim, Y.B. Son, J.Y. Jeong, Y.H. Jo, Comparison of internal waves in various ocean fields around the Korean peninsula. J. Coast. Res. **85**, 466–470 (2018)

41. Y. Silvy, E. Guilyardi, J.B. Sallee, P.J. Durack, Human-induced changes to the global ocean water masses and their time of emergence. Nat. Clim. Change **10**, 1030–1036 (2020)
42. G.C. Li, L.J. Cheng, J. Zhu, K.E. Trenberth, M.E. Mann, J.P. Abraham, Increasing ocean stratification over the past half-century. Nat. Clim. Change **10**, 1116–1123 (2020)
43. H. Schmidt, S. Seitz, E. Hassel, H. Wolf, The density-salinity relation of standard seawater. Ocean Sci. **14**, 15–40 (2018)
44. Y. Qian, Y. Zhao, Q.L. Wu, Y. Yang, Review of salinity measurement technology based on optical fiber sensor. Sens. Actuators B **260**, 86–105 (2018)
45. O. Demir, J.T. Johnson, K.C. Jezek, M. Brogioni, G. Macelloni, L. Kaleschke, L. Brucker, Studies of sea-ice thickness and salinity retrieval using 0.5–2 GHz microwave radiometry. IEEE Trans. Geosci. Remote Sens. **60**, 4304412 (2022)
46. R.A. Cox, F. Culkin, J.P. Riley, The electrical conductivity/chlorinity relationship in natural sea water. Deep Sea Res. I Oceanogr. Res. Pap. **14**, 203–220 (1967)
47. C. Du, S. Zhao, Q. Wang, B. Jia, M. Zhao, L. Zhang, L. Cui, S. Chen, X. Deng, A seawater salinity sensor based on optimized long period fiber grating in the dispersion turning point. Sensors **23**, 4435 (2023)
48. T.H. Kauffmann, M.D. Fontana, Optical sensor of salt concentration: uncertainty evaluation. Sens. Actuators B **161**, 21–27 (2012)
49. B.A. Gozeh, A. Karabulut, A. Yildiz, A. Dere, B. Arif, F. Yakuphanoglu, SILAR controlled CdS nanoparticles sensitized CdO diode based photodetectors. Silicon **12**, 1673–1681 (2020)
50. B. Topaloğlu Aksoy, G. Keşan, E. Özcan, E. Tanrıverdi Eçık, A. Dere, A. Karabulut, F. Yakuphanoglu, B. Çoşut, Solution-processable BODIPY decorated triazine photodiodes and their comprehensive photophysical evaluation. New J. Chem. **44**, 2155–2165 (2020)
51. E. Özcan, B. Topaloğlu Aksoy, E. Tanrıverdi Eçik, A. Dere, A. Karabulut, F. Yakuphanoglu, B. Çoşut, Fabrication of hybrid photodiode systems: BODIPY decorated cyclotriphosphazene covalently grafted graphene oxides. Inorg. Chem. Front. **7**, 2920–2931 (2020)
52. A.G. Al-Sehemi, A. Karabulut, A. Dere, A.A. Al-Ghamdi, F. Yakuphanoglu, Photodiode performance and infrared light sensing capabilities of quaternary Cu_2ZnSnS_4 chalcogenide. Surf. Interfaces **29**, 101802 (2022)
53. C. Taşaltın, T.A. Türkmen, N. Taşaltın, S. Karakuş, Highly sensitive non-enzymatic electrochemical glucose biosensor based on PANI: β12 borophene. J. Mater. Sci.: Mater. Electron. **32**, 10750–10760 (2021)
54. T.A. Türkmen, N. Taşaltın, C. Taşaltın, G. Baytemir, S. Karakuş, PEDOT: PSS/β12 borophene nanocomposites as an inorganic-organic hybrid electrode for high performance supercapacitors. Inorg. Chem. Commun. **139**, 109329 (2022)
55. N. Taşaltın, Borophene Nanocomposite Material and Supercapacitor Containing Borophene Nanocomposite Material WIPO Patent Application WO/2021/201807
56. G. Baytemir, N. Taşaltın, B. Karaca, S. Karakuş, G. Gürsu, B. Barış, D.E. Yıldız, PANI: silicene nanocomposites based non-enzymatic electrochemical voltammetric sensor for dopamine detection. J. Mater. Sci.: Mater. Electron. **34**(17), 1374 (2023)
57. W. Kern, D.A. Puotinen, Cleaning solution based on hydrogen peroxide for use in silicon semiconductor technology. RCA Rev. **31**, 187 (1970)
58. D.E. Yıldız, Ş Altındal, On the temperature dependence of series resistance and interface states in Al/SiO_2/p-Si (MIS) Schottky diodes. Microelectron. Eng. **85**(2), 289–294 (2008). https://doi.org/10.1016/j.mee.2007.06.015
59. B. Barış, M. Yıldırım, S. Karadeniz, A. Karabulut, A. Kose, D.E. Yıldız, Effect of illumination on electrical characteristics of Au/Mn-complex/n-Si photodiode structures. J. Mater. Sci.: Mater. Electron. (2022). https://doi.org/10.1007/s10854-021-07469-y
60. D.E. Yıldız, Ş Altındal, Z. Tekeli, M. Özer, The effects of surface states and series resistance on the performance of Au/SnO_2/n-Si and Al/SnO_2/p-Si (MIS) Schottky barrier diodes. Mater. Sci. Semicond. Process. **13**(1), 34–40 (2010)
61. H.H. Gullu, D.E. Yildiz, Capacitance, conductance, and dielectric characteristics of Al/TiO_2/Si diode. J. Mater. Sci.: Mater. Electron. **32**, 13549–13567 (2021)
62. D.E. Yıldız, S. Karadeniz, H.H. Gullu, A study on electrical properties of Au/4H-SiC Schottky diode under illumination. J. Mater. Sci.: Mater. Electron. **32**(15), 20130–20138 (2021)
63. D.E. Yıldız, H.H. Gullu, H.K. Cavus, Effect of TiO_2 thin film with different dopants in bringing Au-metal into a contact with n-Si. J. Inorg. Organomet. Polym. Mater. **32**(3), 1067–1077 (2022)
64. S.M. Sze, *Physics of Semiconductor Devices*, 2nd edn. (Wiley, New York, 1981)
65. M.D. Bedre, S. Basavaraja, B.D. Salwe, V. Shivakumar, L. Arunkumar, A. Venkataraman, Preparation and characterization of pani and pani-Ag nanocomposites via interfacial polymerization. Polym. Compos. **30**(11), 1668–1677 (2009). https://doi.org/10.1002/pc.20740
66. E.H. Rhoderick, R.H. Williams, *Metal-Semiconductor Contacts*, 2nd edn. (Clarendon Press, Oxford, 1978)
67. D.E. Yildiz, H.H. Gullu, A. Sarilmaz, F. Ozel, A. Kocyigit, M. Yildirim, Dark and illuminated electrical characteristics of Si-based photodiode interlayered with $CuCo_5S_8$ nanocrystals. J. Mater. Sci.: Mater. Electron. **31**, 935–948 (2020)
68. H.H. Gullu, D.E. Yildiz, A. Kocyigit, M. Yıldırım, Electrical properties of Al/PCBM: ZnO/p-Si heterojunction for photodiode application. J. Alloys Compd. **827**, 154279 (2020)
69. S.O. Tan, H.U. Tecimer, O. Çiçek, H. Tecimer, I. Orak, Ş Altındal, Electrical characterizations of Au/ZnO/n-GaAs Schottky diodes under distinct illumination intensities. J. Mater. Sci.: Mater. Electron. **27**, 8340–8347 (2016)
70. E.M. Menyawy, I.T. Zedan, Optical properties and device characteristics of 2-(antipyrin-4-ylhydrazono)-2-(4-nitrophenyl)acetonitrile thin films for photodiode applications. Spectrochim. Acta A **137**, 810 (2015)
71. Ş Karataş, H.M. El-Nasser, A.A. Al-Ghamdi, F. Yakuphanoglu, High photoresponsivity Ru-doped ZnO/p-Si heterojunction diodes by the sol-gel method. Silicon **10**, 651–658 (2018)
72. M. Soylu, M. Cavas, A.A. Al-Ghamdi, Z.H. Gafer, F. El-Tantawy, F. Yakuphanoglu, Photoelectrical characterization of a new generation diode having $GaFeO_3$ interlayer. Sol. Energy Mater. Sol. Cells **124**, 180–185 (2014). https://doi.org/10.1016/j.solmat.2014.01.045
73. M. Soylu, A.A. Al-Ghamdi, F. Yakuphanoglu, Influence of illumination intensity and temperature on the electrical characteristics of an Al/p-GaAs/In structure prepared by thermal evaporation. Microelectron. Eng. **99**, 50 (2012)
74. I.S. Yahia, M. Fadel, G.B. Sakr, F. Yakuphanoglu, S.S. Shenouda, W.A. Farooq, Analysis of current–voltage characteristics of Al/p-$ZnGa_2Se_4$/n-Si nanocrystalline heterojunction diode. J. Alloys Compd. **509**, 4414 (2011)
75. C.R. Crowell, The Richardson constant for thermionic emission in Schottky barrier diodes. Solid State Electron. **8**, 395 (1965)

76. H.H. Gullu, D.E. Yildiz, Analysis of forward and reverse biased current–voltage characteristics of Al/Al_2O_3/n-Si Schottky diode with atomic layer deposited Al_2O_3 thin film interlayer. J. Mater. Sci.: Mater. Electron. **30**, 19383–19393 (2019)
77. P. Chattopadhyay, The effect of shunt resistance on the electrical characteristics of Schottky barrier diodes. J. Phys. D **29**, 823 (1996)
78. M. Cavas, A.A.M. Farag, Z.A. Alahmed, F. Yakuphanouglu, Photosensors based on Ni-doped ZnO/p-Si junction prepared by sol-gel method. Electroceramics **31**, 298–308 (2013)
79. S. Darwish, A.S. Riad, H.S. Soliman, Electrical conductivity and the effect of temperature on photoconduction of n-ZnSe/p-Si rectifying heterojunction cells. Semicond. Sci. Technol. **11**, 96 (1996)
80. S.K. Cheung, N.W. Cheung, Extraction of Schottky diode parameters from forward current-voltage characteristics. Appl. Phys. Lett. **49**, 85 (1986)
81. H.H. Gullu, D.S. Sirin, D.E. Yıldız, Analysis of double Gaussian distribution on barrier inhomogeneity in a Au/n-4H SiC Schottky diode. J. Electron. Mater. **50**(12), 7044–7056 (2021)
82. H.H. Gullu, D.E. Yıldız, S.O. Hacioglu, A. Cirpan, L. Toppare, Dark conduction mechanisms of PTQBDT based heterojunction diode. Phys. Scr. **98**(1), 015819 (2023)
83. M.O. Erdal, Photoresponse properties of coronene nanowires thin-film-based photodiode. J. Mater. Sci.: Mater. Electron. **31**, 18980–18987 (2020)
84. A. Tataroğlu, O. Dayan, N. Özdemir, Z. Şerbetçi, A.A. Al-Ghamdi, A. Dere, F. El-Tantawy, F. Yakuphanoglu, Single crystal ruthenium(II) complex dye based photodiode. Dyes Pigm. **132**, 64–71 (2016)
85. H.H. Gullu, D.E. Yıldız, D.A. Kose, M. Yıldırım, Si-based photosensitive diode with novel Zn-doped nicotinate/nicotinamide mixed complex interlayer. Mater. Sci. Semicond. Process. **147**, 106750 (2022)
86. F. Yakuphanoglu, Transparent metal oxide films-based sensors for solar tracking applications. Composites B **92**, 151–159 (2016)
87. D.E. Yıldız, A. Karabulut, I. Orak, A. Türüt, Effect of atomic layer deposited HfO_2 thin film interfacial layer on the electrical properties of Au/Ti/n-GaAs Schottky diode. J. Mater. Sci.: Mater. Electron. **32**, 10209–10223 (2021)
88. A. Rose, *Concepts in Photoconductivity* (Interscience, New York, 1963)
89. A. Kocyigit, M. Yıldırım, D.A. Kose, D.E. Yıldız, Synthesize and characterization of Co-complex as interlayer for Schottky type photodiode. Polym. Bull. **79**(12), 11389–11408 (2022)
90. D.E. Yıldız, A. Kocyigit, M. Yıldırım, Comparison of Al/TiO_2/p-Si and Al/ZnO/p-Si photodetectors. Opt. Mater. **145**, 114371 (2023)
91. H. Kaçuş, Ç. Çırak, Ş Aydoğan, Effect of illumination intensity on the characteristics of Co/Congo Red/p-Si/Al hybrid photodiode. Appl. Phys. A **126**, 139 (2020)
92. O. Dayan, A.G. Imer, A.G. Al-Sehemi, N. Özdemir, A. Dere, Z. Şerbetçi, A.A. Al-Ghamdi, F. Yakuphanoglu, Photoresponsivity and photodetectivity properties of copper complex-based photodiode. J. Mol. Struct. **1200**, 127062 (2020)
93. W. Choi et al., High-detectivity multilayer MoS_2 phototransistors with spectral response from ultraviolet to infrared. Adv. Mater. **24**, 5832–5836 (2012)
94. L. Wang et al., MoS_2/Si heterojunction with vertically standing layered structure for ultrafast, high-detectivity, self-driven visible-near infrared photodetectors. Adv. Funct. Mater. **25**, 2910–2919 (2015)
95. B.A. Gozeh, A. Karabulut, A. Yildiz, F. Yakuphanoglu, Solar light responsive ZnO nanoparticles adjusted using Cd and La co-dopant photodetector. J. Alloys Compd. **732**, 16–24 (2018)
96. A.S. Dahlan, A. Tataroglu, A.A. Al-Ghamdi, A.A. Al-Ghamdi, S. Bin-Omran, Y. Al-Turki, F. El-Tantawy, F. Yakuphanoglu, Photodiode and photocapacitor properties of Au/CdTe/p-Si/Al device. J. Alloys Compd. **646**, 1151–1156 (2015)
97. R.H. Bube, *Photoconductivity of Solids* (Wiley, New York, 1960)
98. A. Kocyigit, I. Orak, S. Aydogan, Z. Caldıran, A. Turut, Temperature-dependent C-V characteristics of Au/ZnO/n-Si device obtained by atomic layer deposition technique. J. Mater. Sci.: Mater. Electron. **28**, 5880–5886 (2017)
99. L.F. Lai, N. Zainal, C.F. Soon, Fabrication of a diode-based salt solution sensor. Emerg. Adv. Integr. Technol. **1**(1), 10–21 (2020)
100. A.A. Noroozi, Y. Abdi, A graphene/Si Schottky diode for the highly sensitive detection of protein. RSC Adv. **9**, 19613–19619 (2019)
101. T.D. Silva, M. Fawzy, A. Hasani, H. Ghanbari, A. Abnavi, A. Askar, Y. Ling, M.R. Mohammadzadeh, F. Kabir, R. Ahmadi, M. Rosin, K.L. Kavanagh, M.M. Adachi, Ultrasensitive rapid cytokine sensors based on asymmetric geometry two-dimensional MoS_2 diodes. Nat. Commun. **13**, 7593 (2022)

Publisher's Note Springer Nature remains neutral with regard to jurisdictional claims in published maps and institutional affiliations.